applied sciences

MDPI

Article

Evaluation of Frequency Effects on Fatigue Life at High Test Frequencies for SAE 1045 Steel Based on Thermography and Electrical Resistance Measurements

Jonas Anton Ziman [1,*], Fabian Weber [1,2], Janina Koziol [1], Johannes Leon Otto [3], Lukas Maximilian Sauer [3], Frank Walther [3] and Peter Starke [1,2]

[1] Department of Materials Science and Materials Testing (WWHK), Institute QM3, University of Applied Sciences Kaiserslautern, D-67659 Kaiserslautern, Germany; fabian.weber@hs-kl.de (F.W.); janina.koziol@hs-kl.de (J.K.); peter.starke@hs-kl.de (P.S.)
[2] Faculty of Natural Sciences and Technology, Saarland University, D-66123 Saarbrücken, Germany
[3] Chair of Materials Test Engineering (WPT), TU Dortmund University, D-44227 Dortmund, Germany; johannes.otto@tu-dortmund.de (J.L.O.); lukas.sauer@tu-dortmund.de (L.M.S.); frank.walther@tu-dortmund.de (F.W.)
* Correspondence: jonas.ziman@hs-kl.de

Abstract: This research provides a method for a reliable fatigue life estimation at high testing frequencies. The investigations are based on the lifetime prediction method StressLife$_{HCF}$ considering test frequencies of 80 and 260 Hz for normalized SAE 1045 (C45E, 1.1191) steel. Therefore, load increase tests and constant amplitude tests were carried out using a resonant testing rig. To ensure a mechanism-oriented lifetime prediction, the material response to dynamic loading is monitored via temperature and electrical resistance measurements. Due to the higher energy input per time unit, when the test frequency is increased, the heat dissipation also increases. For this reason, a precise differentiation between frequency- and temperature-related effects for adequate fatigue assessment is challenging. To evaluate the temperature's influence on electrical resistance, an electrical resistance-temperature hysteresis is measured, and the frequency influence is analyzed by considering cyclic deformation curves. In addition to an extension of the fatigue life due to an increased test frequency, the lifetime prediction method was validated for high frequencies. The generated S-N curves show a reliable agreement with the data points from conventional constant amplitude tests. In this context, the temperature correction of the electrical resistance proved to be an important input variable for a reliable lifetime prediction.

Keywords: StressLife; fatigue life; lifetime prediction methods; material response; resistivity; frequency; electrical resistance-temperature hysteresis; resonant testing; S-N curves; NDT

Academic Editor: Florent Ravelet

Received: 10 December 2024
Revised: 16 January 2025
Accepted: 18 January 2025
Published: 21 January 2025

Citation: Ziman, J.A.; Weber, F.; Koziol, J.; Otto, J.L.; Sauer, L.M.; Walther, F.; Starke, P. Evaluation of Frequency Effects on Fatigue Life at High Test Frequencies for SAE 1045 Steel Based on Thermography and Electrical Resistance Measurements. *Appl. Sci.* **2025**, *15*, 1022. https://doi.org/10.3390/app15031022

1. Introduction

To describe the relationship between the load amplitude and fatigue life expressed in terms of S-N curves, generally, a large number of specimens and fatigue tests are required. For stress-controlled fatigue tests, a power law relationship, according to Basquin [1], is frequently used to describe S-N curves in the high-cycle fatigue (HCF) regime mathematically, according to Equation (1). The equation consists of the stress amplitude σ_a, the number of cycles to failure N_f, the fatigue strength coefficient σ'_f, and the fatigue strength exponent b.

$$\sigma_a = \sigma'_f \left(2\, N_f\right)^b \quad (1)$$

Usually, fatigue tests in the low-cycle fatigue (LCF) regime are performed while strain-controlled and can be mathematically described by the relationship according to Coffin and Manson [2,3], which is given by Equation (2), using the plastic strain amplitude $\epsilon_{a,p}$, the fatigue ductility coefficient ϵ'_f, and the fatigue ductility exponent c.

$$\epsilon_{a,p} = \epsilon'_f \left(2\, N_f\right)^c \tag{2}$$

The fatigue behaviors in the LCF, HCF, and VHCF (very-high-cycle fatigue) regimes are characterized by significantly differing damage mechanisms [4]. This is especially so for the failure mechanisms in the VHCF regime, which particularly depend on the specific material properties and heat treatment conditions. They are, therefore, crucial as they influence the way cracks initiate and propagate, which is the reason why specific failure mechanisms must be differentiated. Mughrabi distinguishes between type I and II materials. While type I materials tend to be ductile metallic materials without internal defects, type II materials have crack-like defects such as non-metallic inclusions or pores [5,6].

In the HCF and VHCF regimes, type I materials like SAE 1045 (C45E, 1.1191) steel tend to show a microstructural degradation in terms of persistent slip bands (PSB), which reach through grains to the material surface. PSBs are formed when local acting stresses are above a critical threshold value [7,8]. Especially in the VHCF regime, where very high-cycle numbers occur, the stress amplitudes are often below this threshold. Although PSBs typically play a significant role in damage mechanisms, the continuous cyclic loading leads to damage accumulation even at low-stress amplitudes. This accumulation can ultimately result in premature failure of the material.

Investigations referring to the influence of frequency on fatigue behavior have already been carried out by Jenkin in the early 1920s, which showed a significant increase in fatigue life at higher frequencies. Within this research, it was assumed that loads that are sufficient to cause fatigue and fracture for lower frequencies do not have enough time to activate this effect at high test frequencies, and therefore, higher load amplitudes are needed [9]. Studies by Laird and Charsley regarding the frequency effect on cyclic plastic deformation, damage localization, dislocation movement, and fatigue crack growth in pure metals with body-centered cubic (bcc) and face-centered cubic (fcc) structures were performed in the early 1980s [10]. Mayer [11] provided a more detailed review, demonstrating that a frequency effect is differently pronounced depending on the lattice structure of the materials. Pure fcc metals tend to be insensitive regarding an increase in test frequency since the critical shear stress is low and largely unaffected by the strain rate; thus, the slip systems are still active even under high test frequencies. As a result, increased test frequencies have minimal impact on their behavior. In contrast, for pure bcc metals, the high activation energy required for dislocation movement and a greater critical shear stress cause slip systems to become inactive at high frequencies, thus making the frequency effect more pronounced [12,13].

Investigations by Morrissey, McDowell, and Nicholas showed a frequency dependence for different stress ratios concerning the HCF fatigue behavior of Ti-6Al-4V specimens [14]. Hu et al. [15] introduced a new possibility to assess whether a test frequency effect may occur for high-temperature tests by defining a parameter that takes the homologous temperature and material strength into account.

Morrow's research [16] in the 1960s focused on the influence of plastic deformation energy per cycle and its crucial role in the related damage evolution in material. Morrow explored how cyclic loading leads to energy accumulation, contributing to material fatigue over time, and introduced cyclic plastic strain energy as a critical metric for understanding fatigue behavior. Based on his research, damage indicators were defined due to the heat

generation derived from the dissipative energy associated with microstructural deformation mechanisms. These indicators can be derived from direct and indirect temperature measurements and are used to estimate the fatigue strength of metallic materials [17–22]. Building on Morrow's foundational work on cyclic plastic strain energy in fatigue behavior, it is also essential to consider frequency-dependent self-heating in the context of fatigue testing at higher frequencies. At elevated test frequencies, the rapid succession of plastic deformation cycles leads to continuous heat accumulation in the material, as the limited time available for heat dissipation between load cycles restricts heat dissipation [23].

In order to reduce the number of specimens and the required time to provide S-N curves while achieving precise agreement between the calculated and experimental results, various lifetime prediction methods (LPM) [24–32] have been developed recently. The potential of non-destructive testing (NDT), the digitalization of measurement technology, and signal processing are combined in these methods in order to achieve an increased level of information regarding fatigue behavior. Since the generation of S-N curves requires more than 20 tests according to the standard DIN 50100 [33], the previously mentioned methods can demonstrably reduce the associated effort. For instance, high-resolution IR cameras allow microstructure-resolved damage detection, which can be used as a basis for a direct correlation with the degradation evolution of the materials [34,35]. Within the presented research, the frequency dependence of the fatigue life is integrated into a lifetime prediction method based on StressLife, which has been developed in previous research [24,25]. Therefore, this method is used for the first time regarding the increased test frequencies of 80 Hz and 260 Hz.

Apart from temperature-based methods, electrical resistance measurement methods are also well suited for in situ measurements in fatigue tests, even on complex components and structures. Changes in the electrical resistance can directly be correlated with microstructural degradations [36]. This method is appropriate for in situ measurements as well as for determinations in load-free intervals. In addition to the geometry, the electrical resistance depends on the specific electrical resistance, which is made up of temperature-independent and temperature-dependent portions, according to Matthiessen [37], as well as changes during plastic deformation due to variations in defect density [38–40]. Due to the reduction of the effective specimen cross-section, the electrical resistance exhibits a very distinctive sensitivity concerning crack initiation and propagation.

As a consequence of the high self-heating of the specimens caused by the increased test frequency [41], there is a temperature effect on the specimens in addition to a frequency effect. In order to increase the sensitivity with regard to microstructural changes, the temperature-dependent portion of the electrical resistance is minimized within the framework of this research. However, an increased test frequency can result in a considerable reduction in time and costs, but it has a material-dependent influence on fatigue behavior [42]. Therefore, it is necessary to include these aspects in the lifetime prediction for increased test frequencies.

Within this paper, information from an electrical resistance-temperature hysteresis was used to minimize the temperature effects on electrical resistance measurements. The temperature-corrected electrical resistance R_{corr} corresponds to the temperature-independent portions of the specific electrical resistance.

2. Materials and Methods

2.1. Materials

The investigated material is SAE 1045 (C45E, 1.1191) steel in normalized conditions ("+N"), where the heat treatment is characterized by an austenitization at $T_{aust.}$ = 860 °C for $t_{aust.}$ = 45 min. Table 1 summarizes the chemical composition according to our own

measurements obtained by spectrometric element analysis, along with specified limit values according to DIN EN ISO 683-1 [43]. Mechanical properties from tensile tests that were averaged over a total of five tests are summarized in Table 2. For assessing the hardness HV 10 values, nine indents were analyzed, and an average hardness of 178 HV 10 was determined.

Table 1. Chemical composition in wt.-% of the SAE 1045 steel according to DIN EN ISO 683-1 and own analysis.

Material		C	Si	Mn	S	Cr	Mo	Ni
SAE 1045	DIN EN ISO 683-1	0.420–0.500	0.100–0.400	0.500–0.800	≤0.045	≤0.400	≤0.100	≤0.400
	Own analysis (+N)	0.427	0.232	0.742	0.007	0.070	0.020	0.078

Table 2. Mechanical and quasistatic properties of the SAE 1045 steel according to DIN standards and own analysis.

Material		R_m [MPa]	$R_{p0.2}$ [MPa]	A [%]	A_G [%]
SAE 1045	DIN EN ISO 683-1	≥580	≥305	≥16	≥13
	Own analysis (+N)	620	423	26	17

Figure 1 displays micrographs of the specimens' cross-sections (longitudinal and transverse direction) etched with nital by using an Axio Imager.M1m microscope (Carl Zeiss AG, Oberkochen, Germany), showing a ferritic-pearlitic microstructure. The longitudinal section corresponds to the microstructure along the loading axis, while the transversal section is perpendicular to it. Ferrite can be observed as clear, bright grains. Pearlite reveals dark cementite lamellas with bright ferrite in between them. The average grain size obtained by the linear intercept method is approx. d_{grain} = 11 µm. In the longitudinal direction, microstructural banding can be observed (Figure 1a,b), where ferrite and pearlite bands run parallel to the direction of rolling. This banded structure results from a low cooling rate after heat treatment.

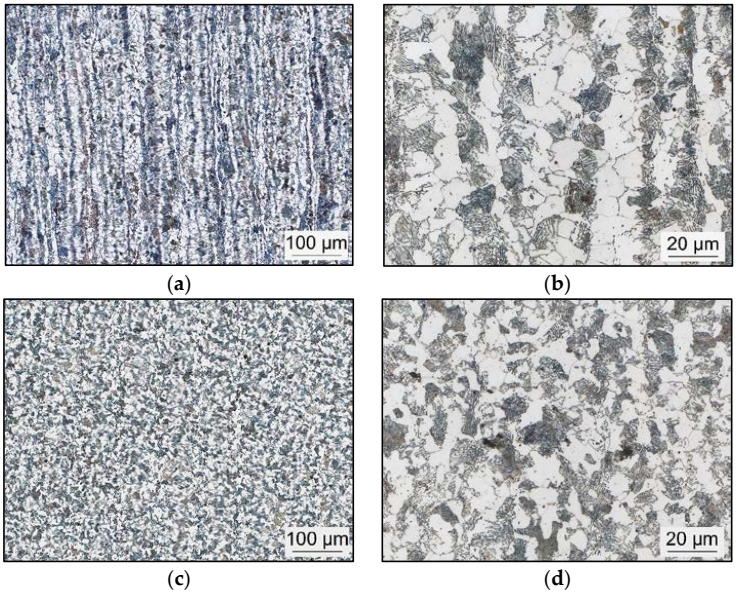

Figure 1. Light micrographs of cross-sections of SAE 1045 specimen in a longitudinal direction with (**a**) 200× magnification and (**b**) 1000× magnification; in a transverse direction with (**c**) 200× magnification and (**d**) 1000× magnification.

To complement the light microscopy images, Figure 2 showcases high-resolution secondary electron (SE) images of the specimens obtained by scanning electron microscopy (SEM) using the TESCAN Clara Mark III (TESCAN, Brno, Czech Republic). The enhanced magnification focuses on the fine alternating ferrite and cementite layers that are characteristic of pearlite, which define its morphology and were not that discernible in the previous light microscopy images.

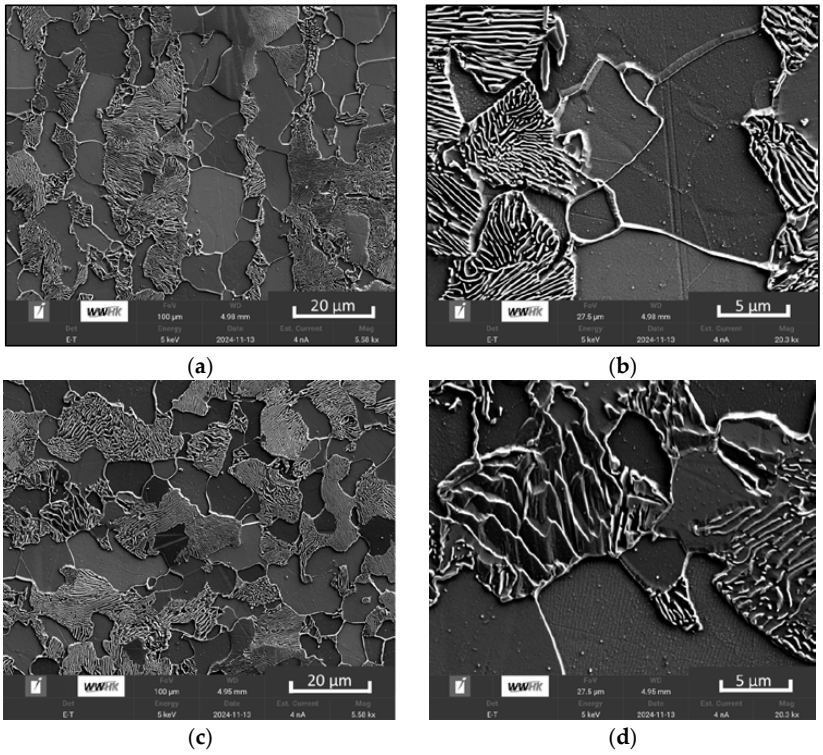

Figure 2. Scanning electron microscopy (SEM) image in secondary electron (SE) mode of cross-sections of SAE 1045 specimen in longitudinal direction with (**a**) 5580× magnification and (**b**) 20,300× magnification; in traverse direction with (**c**) 5580× magnification and (**d**) 20,300× magnification.

The geometry of the fatigue specimens and their dimensions (in mm) are given in Figure 3. A fatigue specimen with a cylindrical gauge length of 15 mm and a gauge diameter of 5.6 mm was chosen to ensure a homogeneous stress distribution in the gauge section and to minimize stress concentrations at the transitions.

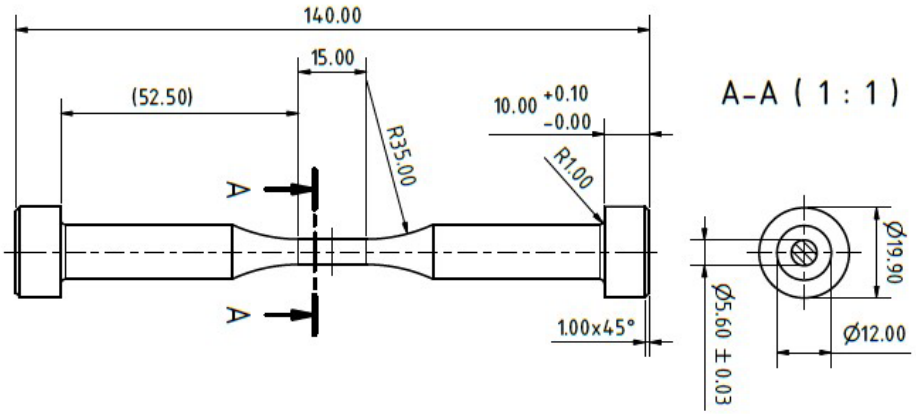

Figure 3. Geometry and dimensions of fatigue specimens.

2.2. StressLife$_{HCF}$ Method

In general, the StressLife$_{HCF}$ method requires two load increase tests (LIT), with the first LIT being used for the basic characterization of the fatigue behavior of the material. LITs enable an estimation of the fatigue strength and provide initial information about the stress amplitude at which a plastic material response can be expected. In general, LITs are performed with a starting stress amplitude $\sigma_{a,start}$ that is evidently below the fatigue strength of the material, with a stepwise increase by $\Delta\sigma_a$ after every ΔN cycle [44]. To cover a large range of stress amplitudes in a reasonable test time, a large increase in the stress amplitude after a defined number of cycles is selected, which, however, leads to a decreased number of data points in the plastic region, as the material fails more quickly due to the high stresses. Therefore, a second LIT with a lower increase in stress amplitude for a more precise assessment of elastic and plastic material behavior is necessary. The material responses of the second LIT are averaged per load level and displayed in a Morrow equivalent plot together with the respective stress amplitude. In this plot, the material response can be divided into a range in which approximately no material response has taken place (elastic area) and a range in which recognizable material responses have occurred (plastic area). With the slopes of the allometric fit functions of these two ranges, the hardening exponent n_{total} for the HCF regime is determined from a weighted average of these slopes. The weighting reflects the proportion of data points in the respective regions. This hardening exponent is used to calculate the fatigue strength exponent b and the fatigue ductility exponent c according to Equations (3) and (4). In addition, the material response M at half of the number of cycles to failure ($0.5 \cdot N_f$) of two constant amplitude tests (CAT) is required to separate the material response into elastic and plastic portions by applying a generalized Coffin and Manson equation and a generalized Basquin equation. The stress amplitudes of the CATs are selected, with one stress amplitude in the specific plastic range and one stress amplitude in the elastic–plastic range of the already performed LIT. However, in this study, only stress amplitudes from the plastic range could be used for the CATs, as previous tests at the given frequencies in the elastic–plastic range had resulted in reaching the maximum number of cycles for the tests without failure (run-outs). In a further step, the coefficients B and C are calculated by Equations (5) and (6). Using a plot based on Ramberg–Osgood, the material response of a calculated constant amplitude test CAT$_{calc}$ can be estimated. This CAT$_{calc}$ is added in conjunction with the two other CATs to the Morrow equivalent plot and is also fitted with an allometric fit function, which allows us to obtain the remaining required parameters, which are used to describe an S-N curve by Equation (7) according to StressLife$_{HCF}$ [25].

$$b = -\frac{n_{total}}{5\, n_{total} + 1} \tag{3}$$

$$c = -\frac{1}{5\, n_{total} + 1} \tag{4}$$

$$C = \frac{\left(2\, N_{f,CAT1}\right)^{b} \cdot M_{CAT2} - \left(2\, N_{f,CAT1}\right)^{b} \cdot M_{CAT1}}{\left(2\, N_{f,CAT2}\right)^{c}} \tag{5}$$

$$B = \frac{M_{CAT1} - C \cdot \left(2\, N_{f,CAT1}\right)^{c}}{\left(2\, N_{f,CAT1}\right)^{b}} \tag{6}$$

$$\sigma_a = K' \cdot \left[B \cdot \left(2\, N_f\right)^{b} + C \cdot \left(2\, N_f\right)^{c}\right]^{n'} \tag{7}$$

2.3. Testing Setup

All CATs and LITs are carried out using a resonant testing rig of the type MIKROTRON (Russenberger Prüfmaschinen AG, Neuhausen am Rheinfall, Switzerland), with a maximum static loading capacity of 20 kN and a maximum force amplitude of 10 kN. The tests were performed with a stress ratio of R = −1 at ambient temperature. According to [25], the specimens' surface temperature was measured in three sections using an IR camera of the type thermoIMAGER TIM QVGA-HD (Micro-Epsilon Messtechnik GmbH & Co., KG, Ortenburg, Germany) with a thermal sensitivity of 0.04 K. In order to avoid non-uniform heating of the specimens during the tests due to the load cell, cooling rings were installed on the upper and lower clamping.

In order to obtain the direct correlation between the change in temperature as a consequence of frequency-induced self-heating effects during the fatigue tests and the measured electrical resistance, a dependency function of these two variables was determined. Therefore, a load-free specimen was heated up to 200 °C by a modified heating device, and the associated change in electrical resistance was measured continuously. The heating device consists of a small opening (d = 7.8 mm) in the center of the gauge length of the specimen. During this procedure, the change in temperature in the middle of the specimen's gauge length was measured by an IR camera, while the electrical resistance R_{total} was traced by using the four-point measuring method consisting of a current feed (3A DC), two Kelvin clamps to measure the drop in voltage on the gauge length, a data acquisition card type NI-9238 (National Instruments, München, Germany), an isolation plate to prevent the flow of current through the machine, and one DC power supply of the type TOE 8851 (Toellner Electronic Instrumente GmbH, Herdecke, Germany) with a setting resolution of 5 mA and a setting accuracy of 0.2% + 10 mA. After reaching 200 °C, a cooling cycle to room temperature followed. Based on the recorded data, a correlation function between the electrical resistance and the change in temperature can be derived. A regression function was used in order to describe the heating path as a square approximation of a second-degree polynomial in accordance with [45]. This setup is shown in Figure 4 and differs only slightly from the measurement setup during the fatigue tests. The current for the fatigue tests was supplied directly at the clamping device instead of additional electrodes, as these could start to vibrate during the tests.

With the use of this regression function, a temperature-dependent electrical resistance value R_{hys} can be calculated by Equation (8), resulting in R_0 as the y-intercept of the regression function. Moreover, ΔT characterizes the change in temperature in the middle of the heating spot, whereas α represents the linear fitting parameter, and β the square fitting parameter. By inserting R_{hys} into Equation (9), a temperature-corrected electrical resistance R_{corr} can be determined, which is unaffected by the temperature flow and is only dependent on microstructural changes, like the formation of dislocations or changes in grain size and grain boundaries [20].

$$R_{hys} = R_0 + \alpha \cdot \Delta T + \beta \cdot \Delta T^2 \tag{8}$$

$$R_{corr} = R_{total} - R_{hys} \tag{9}$$

The electrical resistance-temperature setup is illustrated in Figure 4, together with the result of the hysteresis measurement, including the derived parameters used for the correction of the electrical resistance values in the fatigue tests. Figure 4 depicts the direct relation between the change in temperature and electrical resistance in terms of a hysteresis loop (black curve), with an additional fitting function for the heating path (red curve). In this method, the change in temperature is calculated from the specimen's temperature T during heating and cooling, depending on the initial temperature T_0. The value of the first

fitting parameter refers to the linear temperature coefficient of the material, which has a positive value, as it is characteristic of metals [46]. Due to the fact that all investigated specimens are from the same material batch, the value of the temperature coefficients can be considered constant for the following investigations [47].

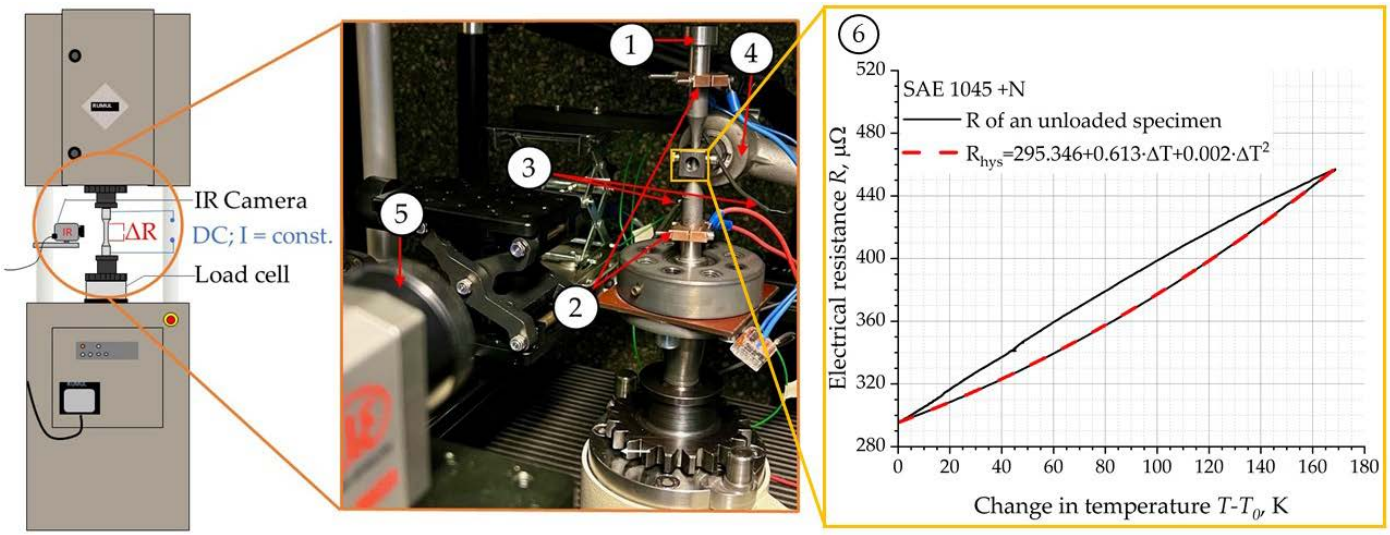

Figure 4. Experimental setup of the resonant testing rig for the determination of the electrical resistance temperature behavior: (1) unloaded fatigue specimen; (2) electrodes for electricity feed; (3) Kelvin clamps to measure the voltage drop; (4) heating device with an adaption for the geometry of the fatigue specimen; (5) IR camera; and (6) electrical resistance-temperature hysteresis, including the fitting (sequence: 30 °C to 200 °C to 30 °C).

3. Results and Discussion

3.1. Load Increase Test

In previous applications of StressLife$_{HCF}$, fatigue tests were carried out at a lower test frequency of 5 Hz [25]. Within this research, the fatigue tests were performed at 80 and 260 Hz, leading to a different progression of the material response in the form of a long-lasting and low-expressed elastic material response and a shorter but very highly expressed plastic response in comparison to the tests at 5 Hz. As discussed in 2.2, two LITs need to be performed. For both test frequencies, an initial LIT with a starting stress amplitude of $\sigma_{a,start}$ = 100 MPa and a load increase of $\Delta\sigma_a$ = 20 MPa after each $\Delta N = 1.8 \times 10^5$ cycles was examined. The increased step length was chosen to ensure comparability of the total duration (in time) to the database of 5 Hz. The same step length was also used for the 260 Hz tests so that no further variations had to be taken into account and to enable a direct correlation of the results.

As given in Figure 5, a starting stress amplitude of $\sigma_{a,start}$ = 180 MPa and a load increase of $\Delta\sigma_a$ = 5 MPa have been defined for the second LIT for both frequencies. Figure 5 shows the cyclic deformation curves of the LITs considering the change in temperature (red), the directly measured change in electrical resistance (green), and the change in R_{corr} (blue), which is derived from the total values calculated by Equations (8) and (9).

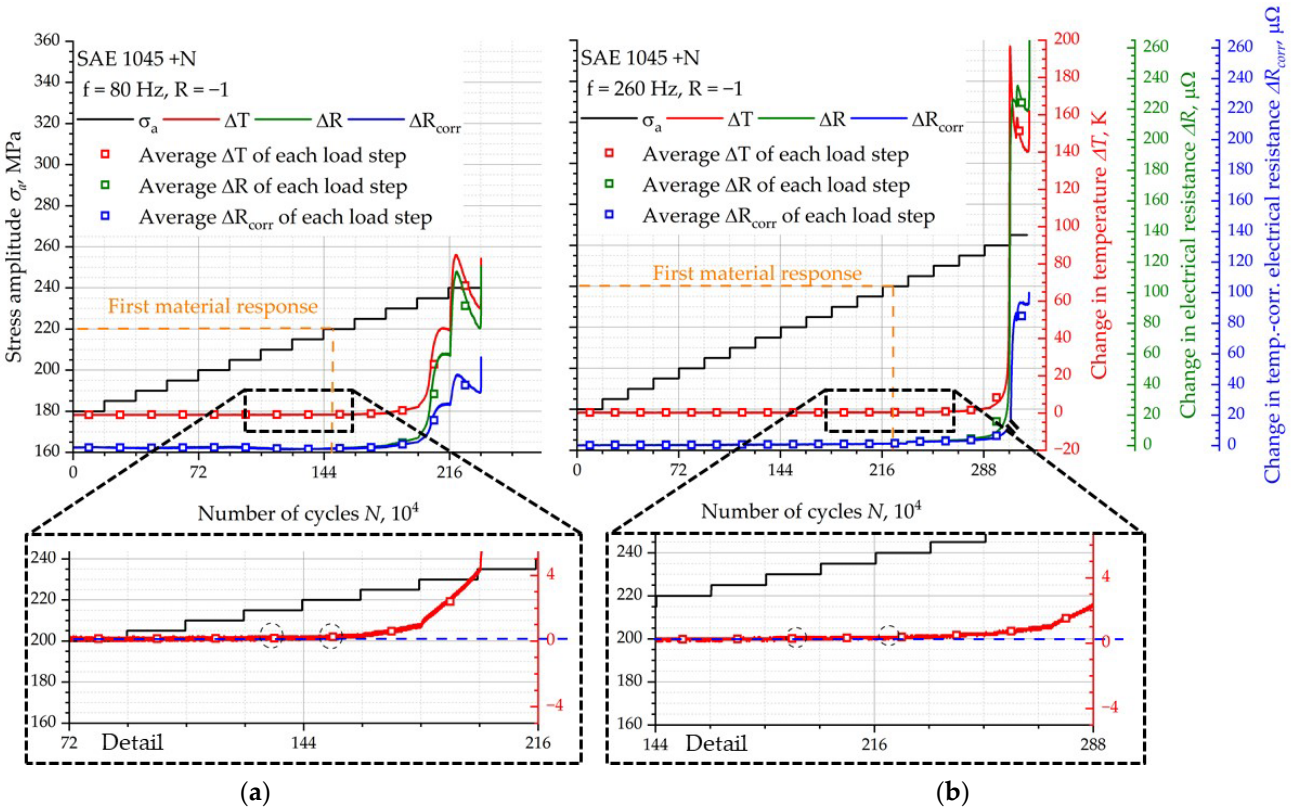

(**a**) (**b**)

Figure 5. Cyclic deformation curves of load increase tests (LIT) for specimens of SAE 1045 +N steel starting at $\sigma_{a,start}$ = 180 MPa with $\Delta\sigma_a$ = 5 MPa and ΔN = 1.8 × 10^5 for (**a**) f = 80 Hz and (**b**) f = 260 Hz.

Since the change in temperature for the LIT at 260 Hz exceeds the fit of the electrical resistance-temperature hysteresis at the beginning of the load stage at 265 MPa, a correction for R_{corr} is not possible for that period, and the graph is displayed with an interruption (black bars). The frequency effect can already be seen in these cyclic deformation curves, represented by a shift in the first material response to higher stress amplitudes (220 MPa for 80 Hz and 240 MPa for 260 Hz), resulting in a higher portion of elastic data points. This first material response can be used to estimate the fatigue strength. The increase in the fatigue strength at higher frequencies can be explained by the fact that the dislocation movement is increasingly limited by the reduced time available for their motion, resulting in reduced plastic deformation in the specimen volume or shift of plastic deformation to higher stress amplitudes at high test frequencies [9]. Another reason is the frequency sensitivity of bcc metals (like ferritic-pearlitic SAE 1045), which are more susceptible to deactivated slip systems due to the high critical shear stress and high dislocation activation energy caused by the high test frequencies [12,13]. At the point where the initial material response occurs, there is no significant change in temperature, indicating that this effect is solely caused by the frequency effect. After the onset of the first material response, both curves show a clear increase in the material response due to the cyclic softening of the material, which is followed by a decrease in the material response in terms of cyclic hardening. In addition, failure of the test frequency of 80 Hz already occurs at 240 MPa, whereas failure at a test frequency of 260 Hz does not occur until 265 MPa.

3.2. Constant Amplitude Test

Due to the general increase in fatigue life, the stress amplitudes selected for the LPM at 260 Hz are also significantly higher compared to those at 80 Hz. The changes in temperature

and electrical resistance are detected as analog to the LITs. The cyclic deformation curves of the CATs are exemplary illustrated for the change in temperature in Figure 6a and for the direct measured electrical resistance R and R_{corr} in Figure 6b. A significantly more pronounced material response in the case of 260 Hz is confirmed in both figures. It should be noted that the data points at $0.5 \cdot N_f$ are highlighted since they are used within the calculations according to $\text{StressLife}_{\text{HCF}}$.

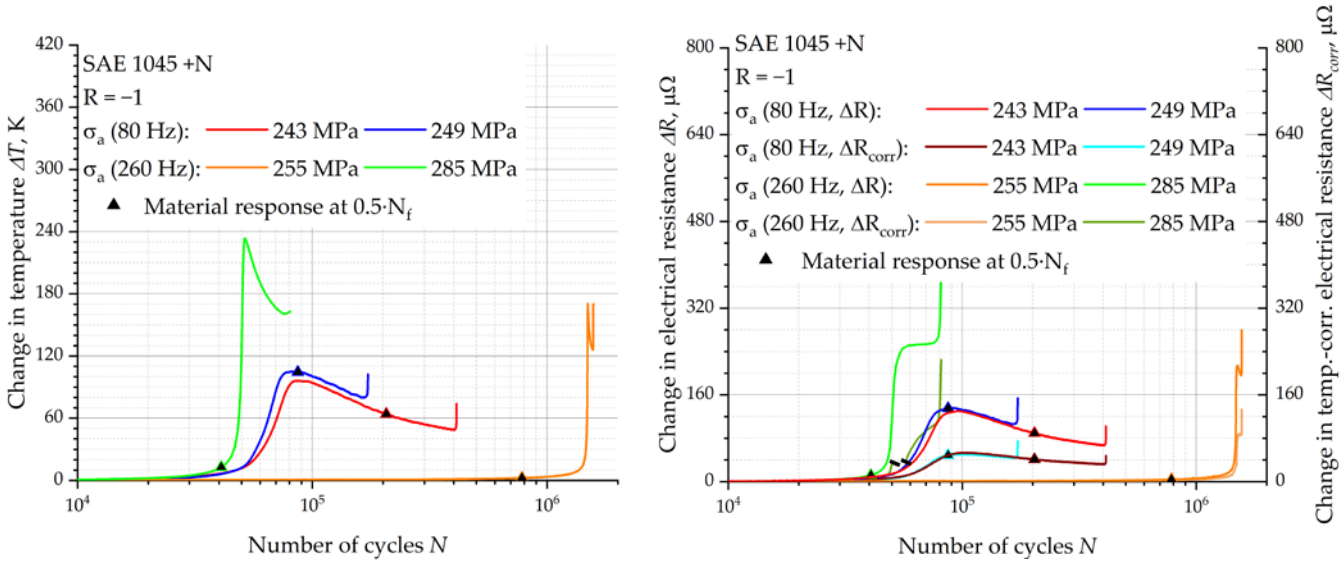

Figure 6. Cyclic deformation curves of constant amplitude tests (CAT) for specimens of SAE 1045 +N steel based on (**a**) change in temperature and (**b**) change in electrical resistance and change in temperature-corrected electrical resistance.

In all fatigue tests, the slope of the increase in R_{corr} is lower than the directly measured electrical resistance.

The point where the maximum cyclic hardening occurs highly depends on the test frequency. While maximum hardening at 80 Hz occurs in a range of approx. 50 % of the fatigue life, it is observed at approx. 76 % of the fatigue life concerning a test frequency of 260 Hz. An explanation for this frequency-related shift has already been given in Section 3.1.

In general, competing processes must be taken into account. On the one hand, more energy per time unit is induced in the specimen due to the increased test frequency, leading to a higher amount of dissipated thermal energy. However, this energy cannot radiate across the specimen quickly enough, and the portion of internal stored heat increases. Due to this, dislocation movement is more facilitated, which tends to shorten the lifetime of the specimens [48]. On the other hand, due to the higher test frequency, it takes considerably longer until the necessary cumulative shear stresses are induced in the microstructure to start the dislocation movements, which tends to extend the lifetime [49]. Depending on the frequency, one of these two effects can dominate, resulting in different cyclic deformation behaviors for different test frequencies. For example, the tests at 80 Hz exhibited a cyclic hardening that extends over a significantly longer cycle range (approx. 10^5 cycles) than at 260 Hz (approx. 3×10^4 cycles). As already explained for the LITs, no temperature correction of the change in electrical resistance is possible for the CAT with a stress amplitude of 285 MPa for a few cycles (Figure 6b), as the change in temperature exceeds 180 K.

3.3. Use of StressLife$_{HCF}$ Within Increased Frequency Fatigue Testing

In this work, the mentioned LPM is applied twice for both test frequencies, once based on the change in temperature and once based on the change in R_{corr}. By using the information from the LIT (Section 3.1), the average material responses of each load level can be obtained and plotted in a Morrow equivalent plot for each test frequency with the respective stress amplitudes, as shown exemplary for R_{corr} in Figure 7.

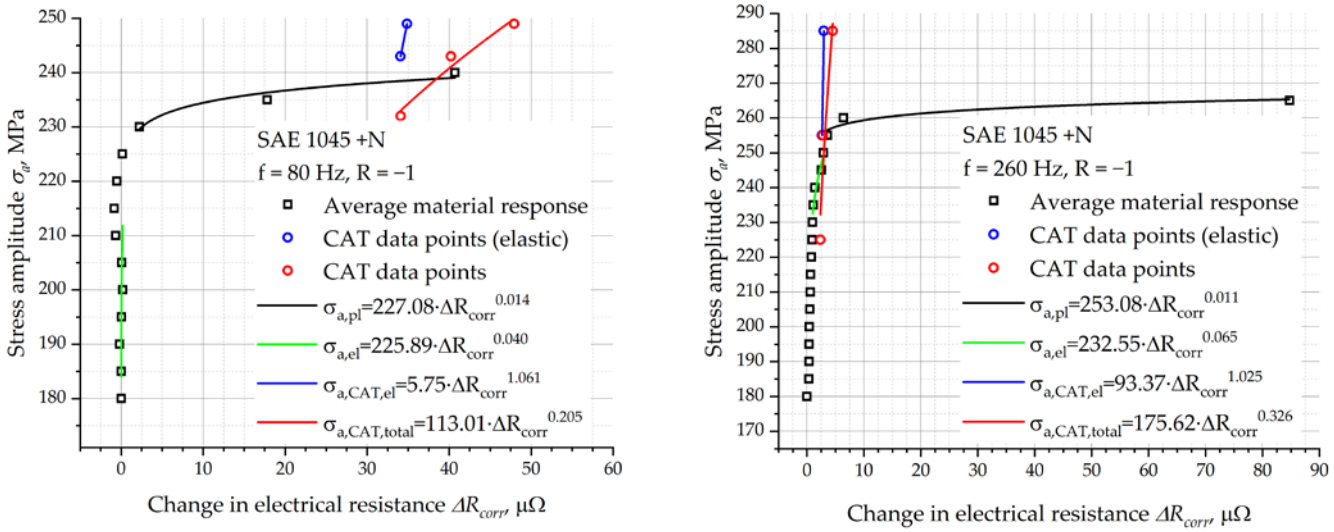

Figure 7. Stress amplitudes vs. average values for the material responses of each load step, including the elastic material responses of both constant amplitude tests (CAT) and the total material responses for a calculated CAT$_{calc}$ according to the StressLife$_{HCF}$ of SAE 1045 +N steel based on the change in temperature-corrected electrical resistance for (**a**) f = 80 Hz and (**b**) f = 260 Hz.

Using the slope of the allometric fits of the elastic (green) and plastic ranges (black) in Figure 7, n_{total} can be calculated for each test frequency by a weighted averaging of the two determined exponents of the fit functions. From the mathematical description given in Equations (3) and (4), the parameters can be determined in the form of the fatigue strength exponent b and the fatigue ductility exponent c [25]. Furthermore, the separation of material response in elastic portions and plastic portions, with the use of a generalized Basquin equation (elastic), a generalized Coffin and Manson equation (plastic), and the fatigue data of two CATs per test frequency from Section 3.2, coefficients B and C are determined according to Equations (5) and (6). This allows the estimation of the material response of a theoretically calculated CAT$_{calc}$. The further final steps for calculating an S-N curve according to StressLife$_{HCF}$ can be found in [24,25,50]. To enable better comparability of the S-N curve based on the change in temperature with the S-N curve based on R_{corr}, both curves are given in Figure 8a for 80 Hz and in Figure 8b for 260 Hz.

Noticeably, both curves in Figure 8a show a precise accuracy with regard to the description of the CAT data points. Furthermore, the fatigue limit, which indicates the maximum stress amplitude under which the material can withstand cyclic loading without failure, can be estimated by the horizontal progression of the curves. This is in line with the observations in Section 3.1, where the fatigue limit is at around 220 MPa for 80 Hz and 240 MPa for 260 Hz according to the load step of the first occurring material response from the LITs in Figure 5 [51].

Furthermore, while the curves in the cycle range from approx. 10^5 cycles for 80 Hz show a very similar course, the curves for 260 Hz differ more clearly. This can be observed from the fatigue lifetime deviation L_D in Table 3, which was determined according to

Equation (10) using the mean fatigue lifetime per stress level $N_{f,val}$ of the validation tests and the calculated fatigue lifetime $N_{f,cal}$ according to StressLife$_{HCF}$. Especially at higher stress amplitudes, the curve based on R_{corr} shows significantly smaller deviations from the validation data points. This can be explained by the different temperatures in 80 Hz (with a max. temperature change in the range of just 100 K) and 260 Hz tests (with a max. temperature change in the range of 250 K). At 260 Hz, temperature changes occur rapidly and may not immediately reflect the microstructural damage due to the material's thermal inertia, which may cause the measured temperature to lag behind the actual microstructural change. As a result, the sensitivity of R_{corr} to local microstructural changes compared to the direct temperature measurement is significantly higher here, offering a more precise correlation with material damage and thus improving the accuracy of the LPM.

$$L_D = \frac{N_{f,cal} - N_{f,val}}{N_{f,val}} \cdot 100\% \quad (10)$$

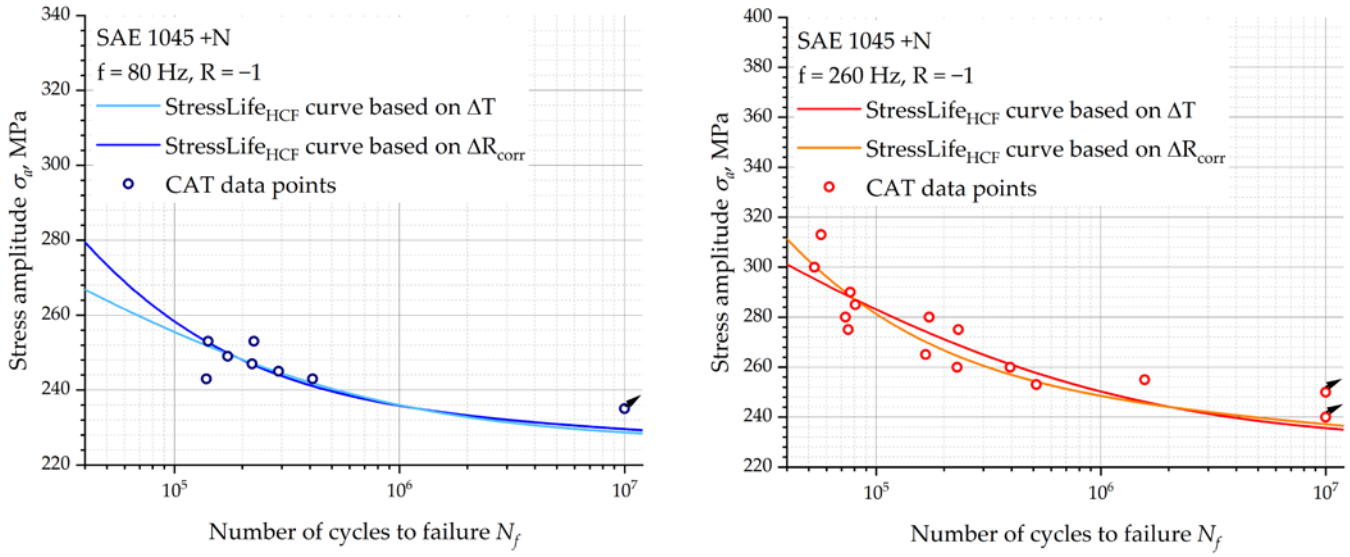

Figure 8. S-N curves according to StressLife$_{HCF}$ for specimens of the SAE 1045 +N steel based on the change in temperature and change in temperature-corrected electrical resistance, including constant amplitude test (CAT) data points for validation for (**a**) f = 80 Hz and (**b**) f = 260 Hz.

Table 3. Deviation of S-N curves according to StressLife$_{HCF}$ from the validation data points for f = 260 Hz.

σ_a [MPa]	313	300	290	285	280	275	265	260	255	253
L_D based on ΔT [%]	−59.26	−20.488	−9.23	12.02	−2.83	3.20	80.85	87.95	−58.86	49.21
L_D based on ΔR_{corr} [%]	−20.59	1.31	−4.52	7.81	−13.87	−15.00	34.05	0.45	−69.50	13.18

In contrast to the calculation based on the change in temperature, the two S-N curves based on the change in R_{corr} in Figure 9 have a similar curve progression from 10^5 to 10^6 cycles, which indicates a successful reduction in the temperature influence on the electrical resistance values. The reduction in temperature influence was already investigated by Wu et al. for a normalized SAE 1045 steel in [52]. Those tests were performed at a test frequency of 5 Hz with additional load-free sequences in order to measure the electrical resistance without the influence of temperature as well as applied load. The

method used in this work can be applied without these sequences, using only an electrical resistance-temperature hysteresis that was determined in advance.

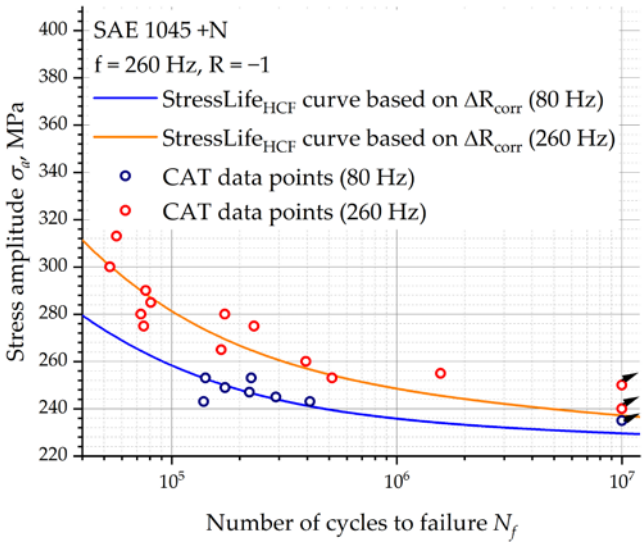

Figure 9. Comparison of the S-N curves according to StressLife$_{HCF}$ for SAE 1045 +N steel based on the change in temperature-corrected electrical resistance for 260 Hz (orange) and 80 Hz (blue), including constant amplitude test (CAT) data points for f = 80 Hz and f = 260 Hz for validation.

The parameters obtained from the StressLife$_{HCF}$ calculations for a test frequency of 80 Hz, as well as the results for a test frequency of 260 Hz, are both summarized in Table 4.

Table 4. Parameters from the StressLife$_{HCF}$ calculation for SAE 1045 +N steel for f = 80 Hz and f = 260 Hz.

Test Frequency [Hz]	Material Response	n'_{total} [-]	b [-]	c [-]	B [K]	C [K]	K' [MPa·K^{-1}]	n' [-]
80	ΔT	0.039	−0.032	−0.839	42.73	3344421.32	184.18	0.065
260	ΔT	0.054	−0.043	−0.786	2.65	127611.30	226.25	0.096
Test Frequency [Hz]	**Material Response**	n'_{total} [-]	b [-]	C [-]	B [μΩ]	C [μΩ]	K' [MPa·μΩ^{-1}]	n' [-]
80	ΔR_{corr}	0.031	−0.026	−0.868	48.85	791644.00	113.01	0.205
260	ΔR_{corr}	0.045	−0.037	−0.817	4.60	27908.99	175.35	0.327

4. Conclusions

Within this research, a lifetime prediction method based on StressLife$_{HCF}$ was validated for the first time regarding the use of higher frequency fatigue testing. It can be stated that the temperature correction of the electrical resistance could be used to separate the influence of frequency-induced self-heating and, therefore, provide a reliable input variable for the StressLife$_{HCF}$ method.

In summary, the following conclusions can be drawn:

1. The StressLifeHCF method is also useful and reliable for test frequencies above 5 Hz. Therefore, an additional calculated value R_{corr} is suitable as a material response for the use of the method to compensate for the temperature influence occurring at high test frequencies.

2. Frequency influences can be seen in cyclic deformation curves of load increase tests, where the first material response shifts to higher stress amplitudes for higher frequencies, resulting in a general extension of fatigue lifetime. For constant amplitude tests, a shift in the position of maximum cyclic softening to higher numbers of cycles at a higher frequency was also observed.
3. Competing processes must be taken into account during higher frequency fatigue. On the one hand, processes that reduce the fatigue lifetime due to heat build-up resulting in very high temperatures of the specimen have an effect by increasing the dislocation mobility. On the other hand, lifetime-extending processes have an effect, as the dislocation movement is slowed down due to the high test frequencies.

In future research, different fatigue life stages will be investigated by means of scanning electron microscopy and X-ray imaging to better understand the frequency-induced microstructure evolution, which is crucial for identifying frequency-related damage mechanisms and may also be implemented into the lifetime prediction method. The goal is to obtain S-N curves for further test frequencies from the $\text{StressLife}_{\text{HCF}}$ calculation using only just one test frequency without having to execute additional tests at other frequencies. To enable this conversion, a factor could be determined based on the frequency difference. Since the electrical resistance-temperature hysteresis is acquired without dynamic stress in a quasistatic system, the behavior may vary in a dynamic system. For this reason, air cooling will be installed for future tests to counteract the forming heat build-up and to reduce the temperature effects. Also, the test bench must be adapted to obtain higher temperatures in the hysteresis by using a more powerful or comparable heat source. The $\text{StressLife}_{\text{HCF}}$ method at high test frequencies should also be verified with different heat treatment conditions, austenitic materials, and further material groups. As a result of the increasing importance of additively manufactured materials, an application to this type of material appears highly relevant.

Author Contributions: Conceptualization, J.A.Z.; methodology, J.A.Z.; validation, J.A.Z.; formal analysis, J.A.Z. and F.W. (Fabian Weber); investigation, J.A.Z., J.L.O., J.K. and L.M.S.; resources, F.W. (Frank Walther) and P.S.; data curation, J.A.Z. and J.K.; writing—original draft preparation, J.A.Z.; writing—review and editing, J.A.Z., F.W. (Fabian Weber), J.K., J.L.O., L.M.S., F.W. (Frank Walther) and P.S.; visualization, J.A.Z. and J.K.; supervision, F.W. (Frank Walther) and P.S.; project administration, J.A.Z. and J.L.O.; funding acquisition, F.W. (Frank Walther) and P.S. All authors have read and agreed to the published version of the manuscript.

Funding: This research was funded by the German Research Foundation (Deutsche Forschungsgemeinschaft DFG), project no. 518776466 (STA 1133/22-1, WA 1672/120-1).

Institutional Review Board Statement: Not applicable.

Informed Consent Statement: Not applicable.

Data Availability Statement: The raw data supporting the conclusions of this article will be made available by the authors on request.

Acknowledgments: The authors would like to thank the German Research Foundation (Deutsche Forschungsgemeinschaft, DFG) for their financial support of this research project (project no. 518776466) and for providing the resonant test rig (project no. 468976436, INST 252/21-1 FUGG) as well as the scanning electron microscope (project no. 514139564, INST 252/27-1) at the University of Applied Sciences Kaiserslautern. Additional thanks to the University of Applied Sciences Kaiserslautern for their financial support in procuring the test infrastructure. Thanks to Hanna Jost and Moritz Maul for their support in the experimental investigations within their masters' theses. The authors are grateful to Russenberger Prüfmaschinen AG for their technical support.

Conflicts of Interest: The authors declare no conflicts of interest.

References

1. Basquin, O.H. The Exponential Law on Endurance Tests. *ASTM Proc.* **1910**, *10*, 625–630.
2. Coffin, L.F. A Study of the Effects of Cyclic Thermal Stresses on a Ductile Metal. *J. Fluids Eng.* **1954**, *76*, 931–949. [CrossRef]
3. Manson, S.S. *Behavior of Materials under Conditions of Thermal Stress*; University of Michigan: Ann Arbor, MI, USA, 1953.
4. Hong, Y.; Sun, C. The Nature and the Mechanism of Crack Initiation and Early Growth for Very-High-Cycle Fatigue of Metallic Materials–An Overview. *Theor. Appl. Fract. Mech.* **2017**, *92*, 331–350. [CrossRef]
5. Mughrabi, H. Specific Features and Mechanisms of Fatigue in the Ultrahigh-Cycle Regime. *Int. J. Fatigue* **2006**, *28*, 1501–1508. [CrossRef]
6. Mughrabi, H. On 'Multi-stage' Fatigue Life Diagrams and the Relevant Life-controlling Mechanisms in Ultrahigh-cycle Fatigue. *Fatigue Fract. Eng. Mater. Struct.* **2002**, *25*, 755–764. [CrossRef]
7. Mughrabi, H.; Ackermann, F.; Herz, K. Persistent Slipbands in Fatigued Face-Centered and Body-Centered Cubic Metals. In *Fatigue Mechanisms*; ASTM International: West Conshohocken, PA, USA, 19428-2959; 1979; pp. 69–105.
8. Meng, F.; Ferrié, E.; Déprés, C.; Fivel, M. 3D Discrete Dislocation Dynamic Investigations of Persistent Slip Band Formation in FCC Metals under Cyclical Deformation. *Int. J. Fatigue* **2021**, *149*, 106234. [CrossRef]
9. Jenkin, C.F. High-Frequency Fatigue Tests. *Proc. R. Soc. Lond. Ser. A Contain. Pap. A Math. Phys. Character* **1925**, *109*, 119–143. [CrossRef]
10. Laird, C.; Charsley, P. Strain Rate Sensitivity Effects in Cyclic Deformation and Fatigue Crack. In *Proceedings of 1st International Conference on Corrosion Fatigue up to Ultrasonic Frequencies, 25–30 October 1981*; The Metall Soc of AIME: Philadelphia, PA, USA, 1982; pp. 187–205.
11. Mayer, H. Fatigue Crack Growth and Threshold Measurements at Very High Frequencies. *Int. Mater. Rev.* **2012**, *44*, 1–34. [CrossRef]
12. Zhao, A.; Xie, J.; Sun, C.; Lei, Z.; Hong, Y. Effects of Strength Level and Loading Frequency on Very-High-Cycle Fatigue Behavior for a Bearing Steel. *Int. J. Fatigue* **2012**, *38*, 46–56. [CrossRef]
13. Papakyriacou, M.; Mayer, H.; Pypen, C.; Plenk, H.; Stanzl-Tschegg, S. Influence of Loading Frequency on High Cycle Fatigue Properties of b.c.c. and h.c.p. Metals. *Mater. Sci. Eng. A* **2001**, *308*, 143–152. [CrossRef]
14. Morrissey, R.J.; McDowell, D.L.; Nicholas, T. Frequency and Stress Ratio Effects in High Cycle Fatigue of Ti-6Al-4V. *Int. J. Fatigue* **1999**, *21*, 679–685. [CrossRef]
15. Hu, Y.; Sun, C.; Xie, J.; Hong, Y. Effects of Loading Frequency and Loading Type on High-Cycle and Very-High-Cycle Fatigue of a High-Strength Steel. *Materials* **2018**, *11*, 1456. [CrossRef] [PubMed]
16. Morrow, J. Cyclic Plastic Strain Energy and Fatigue of Metals. In *Proceedings of the A Symposium Presented at the Sixty-Seventh Annual Meeting American Society for Testing and Materials, STP 378*; Lazan, B., Ed.; ASTM International: Chicago, IL, USA, 1964; pp. 45–87.
17. Schelp, M.; Eifler, D. Evaluation of the HCF-Behavior of 42CrMoS4 by Means of Strain, Temperature and Electrical Measurements. *Mater. Sci. Eng. A* **2001**, *319–321*, 652–656. [CrossRef]
18. Fargione, G.; Geraci, A.; La Rosa, G.; Risitano, A. Rapid Determination of the Fatigue Curve by the Thermographic Method. *Int. J. Fatigue* **2002**, *24*, 11–19. [CrossRef]
19. Doudard, C.; Calloch, S.; Hild, F.; Cugy, P.; Galtier, A. Identification of the Scatter in High Cycle Fatigue from Temperature Measurements. *Comptes Rendus Mec.* **2004**, *332*, 795–801. [CrossRef]
20. Eifler, D.; Piotrowski, A. Bewertung Zyklischer Verformungsvorgänge Metallischer Werkstoffe Mit Hilfe Mechanischer, Thermometrischer Und Elektrischer Messverfahren (Characterization of Cyclic Deformation Behaviour by Mechanical, Thermometrical and Electrical Methods. *Mater. Werkst.* **1995**, *26*, 121–127. [CrossRef]
21. Dengel, D.; Harig, H. Estimation of the Fatigue Limit by Progressively-Increasing Load Tests. *Fatigue Fract. Eng. Mater. Struct.* **1980**, *3*, 113–128. [CrossRef]
22. Mehdizadeh, M.; Haghshenas, A.; Khonsari, M.M. In-Situ Technique for Fatigue Life Prediction of Metals Based on Temperature Evolution. *Int. J. Mech. Sci.* **2021**, *192*, 106113. [CrossRef]
23. Wu, X.; Li, L. An Overview of Self-Heating Phenomena and Theory Related to Damping and Fatigue of Metals. *Appl. Sci.* **2022**, *12*, 3054. [CrossRef]
24. Starke, P. StressLifetc–NDT-Related Assessment of the Fatigue Life of Metallic Materials. *Mater. Test.* **2019**, *61*, 297–303. [CrossRef]
25. Weber, F.; Koziol, J.; Starke, P. StressLife: A Short-Time Approach for the Determination of a Trend S-N Curve in and beyond the HCF Regime for the Steels 20MnMoNi5-5 and SAE 1045. *Materials* **2023**, *16*, 3914. [CrossRef] [PubMed]
26. Wu, H.; Bäumchen, A.; Engel, A.; Acosta, R.; Boller, C.; Starke, P. SteBLife–A New Short-Time Procedure for the Evaluation of Fatigue Data. *Int. J. Fatigue* **2019**, *124*, 82–88. [CrossRef]

27. Wu, H.; Ziman, J.A.; Raghuraman, S.R.; Nebel, J.-E.; Weber, F.; Starke, P. Short-Time Fatigue Life Estimation for Heat Treated Low Carbon Steels by Applying Electrical Resistance and Magnetic Barkhausen Noise. *Materials* **2022**, *16*, 32. [CrossRef] [PubMed]
28. Weber, F.; Wu, H.; Starke, P. A New Short-Time Procedure for Fatigue Life Evaluation Based on the Linear Damage Accumulation by Palmgren–Miner. *Int. J. Fatigue* **2023**, *172*, 107653. [CrossRef]
29. Theil, N. Fatigue Life Prediction Method for the Practical Engineering Use Taking in Account the Effect of the Overload Blocks. *Int. J. Fatigue* **2016**, *90*, 23–35. [CrossRef]
30. Liu, J.; Liu, X. An Improved Method for Fatigue Life Prediction of Metal Materials Based on Thermodynamic Entropy. *Int. J. Fatigue* **2023**, *170*, 107546. [CrossRef]
31. Liu, Y.-K.; Fan, J.-L.; Zhu, G.; Zhu, M.-L.; Xuan, F.-Z. Data-Driven Approach to Very High Cycle Fatigue Life Prediction. *Eng. Fract. Mech.* **2023**, *292*, 109630. [CrossRef]
32. Jiang, W.; Xie, X.; Wang, T.; Zhang, X.; Tu, S.-T.; Wang, J.; Zhao, X. Fatigue Life Prediction of 316L Stainless Steel Weld Joint Including the Role of Residual Stress and Its Evolution: Experimental and Modelling. *Int. J. Fatigue* **2021**, *143*, 105997. [CrossRef]
33. *DIN 50100:2016-12*; Schwingfestigkeitsversuch-Durchführung Und Auswertung von Zyklischen Versuchen Mit Konstanter Lastamplitude Für Metallische Werkstoffproben Und Bauteile. 2016. Available online: https://www.dinmedia.de/de/norm/din-50100/263107018 (accessed on 20 January 2025).
34. Zhao, Y.; Lin, Z.; Xia, Y.; Chen, L.; Gu, G.; Pan, L. Fatigue-Limit Assessment via Infrared Thermography for a High-Strength Steel. *Materials* **2025**, *18*, 279. [CrossRef]
35. Cappello, R.; Meneghetti, G.; Ricotta, M.; Pitarresi, G. On the Correlation of Temperature Harmonic Content with Energy Dissipation in C45 Steel Samples under Fatigue Loading. *Mech. Mater.* **2022**, *168*, 104271. [CrossRef]
36. Sauer, L.M.; Otto, J.L.; Ziman, J.A.; Starke, P.; Walther, F. Test Setup for Analyzing the Electrical Resistance during Fatigue Loading for Metastable Austenite AISI 304L and Its Diffusion-Brazed Joints. *J. Mater. Res. Technol.* **2025**, *35*, 535–544. [CrossRef]
37. Matthiessen, A. On the Specific Resistance of the Metals in Terms of the B. A. Unit (1864) of Electric Resistance, Together with Some Remarks on the so-Called Mercury Unit. *London, Edinb. Dublin Philos. Mag. J. Sci.* **1865**, *29*, 361–370. [CrossRef]
38. Omari, M.A.; Sevostianov, I. Evaluation of the Growth of Dislocations Density in Fatigue Loading Process via Electrical Resistivity Measurements. *Int. J. Fract.* **2013**, *179*, 229–235. [CrossRef]
39. Glushko, O.; Cordill, M.J. Electrical Resistance Decrease Due to Grain Coarsening Under Cyclic Deformation. *JOM* **2014**, *66*, 598–601. [CrossRef]
40. Sun, B.; Yang, L.; Guo, Y. A High-Cycle Fatigue Accumulation Model Based on Electrical Resistance for Structural Steels. *Fatigue Fract. Eng. Mater. Struct.* **2007**, *30*, 1052–1062. [CrossRef]
41. Guo, Q.; Zaïri, F.; Yang, W. Evaluation of Intrinsic Dissipation Based on Self-Heating Effect in High-Cycle Metal Fatigue. *Int. J. Fatigue* **2020**, *139*, 105653. [CrossRef]
42. Yakovleva, T.Y.; Matokhnyuk, L.E. Prediction of Fatigue Characteristics of Metals at Different Loading Frequences. *Strength Mater.* **2004**, *36*, 442–448. [CrossRef]
43. *DIN EN ISO 683-1*; Heat-Treatable Steels, Alloy Steels and Free-Cutting Steels—Part 1: Non-Alloy Steels for Quenching and Tempering. International Organization for Standardization: Geneva, Switzerland, 2016.
44. Walther, F. Microstructure-Oriented Fatigue Assessment of Construction Materials and Joints Using Short-Time Load Increase Procedure. *Mater. Test.* **2014**, *56*, 519–527. [CrossRef]
45. Harriehausen, T.; Schwarzenau, D. *Moeller Grundlagen Der Elektrotechnik*; Springer Fachmedien Wiesbaden: Wiesbaden, Germany, 2019; ISBN 978-3-658-27839-7.
46. Stiny, L. *Passive Elektronische Bauelemente: Aufbau, Funktion, Eigenschaften, Dimensionierung Und Anwendung*, 3rd ed.; Springer Fachmedien Wiesbaden: Wiesbaden, Germany, 2019; ISBN 978-3-658-24732-4.
47. Dellinger, J.H. *The Temperature Coefficient of Resistance of Copper*, 1st ed.; U.S. Department of Commerce and Labor, Bureau of Standards, University of Michigan: Ann Arbor, MI, USA, 1911; Volume 147.
48. Hong, Y.; Hu, Y.; Zhao, A. Effects of Loading Frequency on Fatigue Behavior of Metallic Materials—A Literature Review. *Fatigue Fract. Eng. Mater. Struct.* **2023**, *46*, 3077–3098. [CrossRef]
49. Tahmasbi, K.; Alharthi, F.; Webster, G.; Haghshenas, M. Dynamic Frequency-Dependent Fatigue Damage in Metals: A State-of-the-Art Review. *Forces Mech.* **2023**, *10*, 100167. [CrossRef]
50. Aeran, A.; Acosta, R.; Siriwardane, S.C.; Starke, P.; Mikkelsen, O.; Langen, I.; Walther, F. A Nonlinear Fatigue Damage Model: Comparison with Experimental Damage Evolution of S355 (SAE 1020) Structural Steel and Application to Offshore Jacket Structures. *Int. J. Fatigue* **2020**, *135*, 105568. [CrossRef]

51. Kucharczyk, P.; Rizos, A.; Münstermann, S.; Bleck, W. Estimation of the Endurance Fatigue Limit for Structural Steel in Load Increasing Tests at Low Temperature. *Fatigue Fract. Eng. Mater. Struct.* **2012**, *35*, 628–637. [CrossRef]
52. Wu, H.; Bill, T.; Teng, Z.J.; Pramanik, S.; Hoyer, K.-P.; Schaper, M.; Starke, P. Characterization of the Fatigue Behaviour for SAE 1045 Steel without and with Load-Free Sequences Based on Non-Destructive, X-Ray Diffraction and Transmission Electron Microscopic Investigations. *Mater. Sci. Eng. A* **2020**, *794*, 139597. [CrossRef]